



Pergamon

Acta mater. 48 (2000) 4797–4811



www.elsevier.com/locate/actamat

COMPLETE EXPERIMENTAL TEST OF KINETIC MODELS FOR RAPID ALLOY SOLIDIFICATION

J. A. KITTL*¹, P. G. SANDERS[†], M. J. AZIZ¹§, D. P. BRUNCO[¶]² and M. O. THOMPSON²

¹Division of Engineering and Applied Sciences, Harvard University, Pierce Hall, 29 Oxford Street, Cambridge, MA, USA and ²Department of Materials Science and Engineering, Cornell University, Ithaca, NY, USA

(Received 19 April 2000; received in revised form 24 July 2000; accepted 3 August 2000)

Abstract—The interface response functions for rapid solidification of a non-dilute binary alloy were measured in the regime of partial solute trapping, where substantial discrepancies exist among predictions for the interfacial undercooling in various models. We used pulsed laser melting of Si-As on insulating substrates to enforce planar solidification spanning the velocity range 0.2–2 m/s. Nanosecond-resolution electrical measurements of the time-dependent melt depth and of the electrical resistivity of a buried Pt thin film thermometer permitted us to determine the solidification velocity and the temperature of the crystal/melt interface. With composition–depth profile measurements we also determined the nonequilibrium partition coefficient. The measured velocity-dependence of the interface temperature and partition coefficient are quantitatively consistent with the continuous growth model without solute drag of M. J. Aziz and T. Kaplan [Acta Metall. **36**, 1335 (1988)] and are qualitatively and quantitatively inconsistent with all models exhibiting a significant solute drag effect. Elements of a potential explanation are proposed using the solute drag model of M. Hillert and B. Sundman [Acta Metall. **24**, 731 (1976)] to investigate the origin of the solute drag effect in terms of irreversible processes occurring within a diffuse interface. © 2000 Acta Metallurgica Inc. Published by Elsevier Science Ltd. All rights reserved.

Keywords: Rapid solidification; Kinetics; Phase transformations; Laser annealing

1. INTRODUCTION

The kinetics of interface-mediated phase transformations have been the subject of considerable theoretical and experimental research. In the study of the phenomenology and mechanisms associated with nonequilibrium interface kinetics, rapid alloy solidification has been frequently used as a prototypical case because of the simplifications resulting from the lack of coherency stress effects and, for systems with an atomically rough interface, from the simple interface structure. In solidification the phase selection, growth velocity, chemical composition, long and short range order, and microstructure of a growing phase are highly dependent on the local conditions at the crystal/melt interface, e.g. temperature, composition, orientation, curvature, interface structure. The objective of kinetic models is to per-

mit the understanding of these dependencies and ultimately to impart predictive capability for the production of materials and microstructures under solidification processing and other nonequilibrium conditions. At slow solidification rates, the assumption of local equilibrium at the crystal/melt interface is valid. However, local equilibrium is not maintained during rapid solidification [1], for which models of nonequilibrium interface kinetics abound but definitive measurements are rare. Substantial deviations from local equilibrium for solidification set in as the interface velocity approaches the diffusive speed v_D — the ratio of the diffusion coefficient across the interface to the interatomic spacing [2]. Measured diffusive speeds for solidification [2, 3] fall in the range 100 ± 2 m/s. The issue of local interfacial equilibrium often also arises during solid–solid transformations, where the diffusive speed as defined above is expected to be much smaller.

For binary alloys the nonequilibrium interface response functions [4] predict (i) the composition (mole fraction of solute) X_S of the growing solid (or “solute trapping function”), and (ii) the velocity v of

* Present address: Texas Instruments Inc., Dallas TX.

† Present address: Ford Motor Company, Dearborn, MI.

§ To whom all correspondence should be addressed. Tel.: +1-617-495-9884.

E-mail address: maziz@harvard.edu (M.J. Aziz)

¶ Present address: Intel Corporation, Santa Clara, CA.

the interface (or “velocity-undercooling function”); in terms of the interface temperature T_i and composition X_L of the liquid at the interface. The validity of existing models can be assessed by experimental characterization of both interface response functions in planar binary alloy solidification.

For dilute alloys the interface response functions simplify. The velocity-undercooling function becomes indistinguishable from that of the pure solvent [5] and the solute trapping function can be described by a velocity-dependent but temperature- and composition-independent ratio, the partition coefficient $k \equiv X_S/X_L$. In this limit the solute trapping function has been measured extensively [6]. In the non-dilute case, however, solute trapping measurements only partially test models, leaving the velocity-undercooling function unresolved. A complete test requires the experimental determination of T_i as well as of v and k . In particular, measurements of the velocity-undercooling function for concentrated alloys can determine whether or not the interface is slowed by a solute drag effect predicted by some models [7–9].

1.1. Models

During solidification of a pure element with an atomically rough interface, the velocity-undercooling function in the low-velocity, linear regime is commonly modeled as

$$v = \frac{v_C(T_i)}{RT_i}(-\Delta G_{\text{eff}}) \quad (1)$$

where $v_C(T_i)$ is a kinetic coefficient that is often expected to have Arrhenius form, R is the gas constant, and, for pure elements, ΔG_{eff} is a molar Gibbs free energy change effectively driving solidification ($\Delta G_{\text{eff}} < 0$ and $v > 0$ for solidification). Although models extend to the nonlinear behavior at large deviations from equilibrium [10], for most cases — including those of concern to us in this study — only the linear behavior near equilibrium ($v/v_C \ll 1$) is important.

This relation has been extended to alloys using sharp interface and continuum models. The sharp interface models include the Aziz–Kaplan continuous growth model (CGM) both with and without solute drag [8] and the Ågren [9] model. Continuum approaches include the Hillert–Sundman (H–S) [7, 11] and the Baker model [12]. In the CGM without solute drag it is postulated that equation (1) applies with

$$\Delta G_{\text{eff}} = \Delta G_{\text{DF}} \equiv X_S \Delta \mu_B + (1 - X_S) \Delta \mu_A, \quad (2)$$

where the “driving free energy” ΔG_{DF} is the change in Gibbs free energy per mole solidified, and $\Delta \mu_B$ and

$\Delta \mu_A$ are the changes in chemical potential upon solidification for solute and solvent respectively. Hence in the linear regime in the CGM without solute drag, the velocity is proportional to the driving free energy. In the CGM with solute drag, the free energy ΔG_D dissipated by solute-solvent redistribution affects the velocity, and it is postulated that equation (1) applies with

$$(-\Delta G_{\text{eff}}) = (-\Delta G_{\text{DF}}) - (\Delta G_D) \quad (3)$$

where, for clarity, equation (3) is written so all quantities in parentheses are positive for solidification. For a sharp interface model such as the CGM with solute drag,

$$\Delta G_D = (X_L - X_S)(\Delta \mu_B - \Delta \mu_A). \quad (4)$$

The compositions are determined by the solute trapping function. The non-dilute CGM expression for the partition coefficient is obtained [8] from a solute-solvent redistribution flux vs. driving force for redistribution relation whose nonlinear behavior at large driving forces cannot be neglected for these experiments. The result is

$$k = \frac{\kappa_e + (v/v_D)}{1 + (v/v_D) - (1 - \kappa_e)X_L}, \quad (5)$$

where the equilibrium partitioning parameter κ_e is defined as

$$\kappa_e(X_L, X_S, T_i) \equiv \left(\frac{X_S}{X_L} \right) \exp \left[-\frac{\Delta \mu_B - \Delta \mu_A}{RT_i} \right]. \quad (6)$$

In the dilute limit, equation (5) reduces to

$$k(v) = \frac{k_e + (v/v_D)}{1 + (v/v_D)}, \quad (7)$$

where k_e is the equilibrium partition coefficient.

In another sharp interface model due to Ågren [9], ΔG_D is given by half the right hand side of equation (4) and the partition coefficient is obtained from a solute-solvent redistribution flux-driving force relation similar to that in the CGM except that linear behavior characteristic of small driving forces is assumed to hold at all driving forces.

Continuum models assume that the crystal/melt interface has a finite thickness. The concentration profile across the interface is determined by solving the diffusion equation for non-dilute solutions [11] under steady state conditions in a reference frame fixed on the interface:

$$v(X(z)-X_S) + D(z)\frac{X(z)(1-X(z))}{RT_i} \frac{d}{dz}(\mu_B - \mu_A) = 0, \quad (8)$$

with z the coordinate normal to the interface and $D(z)$ the local tracer diffusivity. In this case, ΔG_D is given by [8]

$$\Delta G_D = -\int_0^\delta (X(z)-X_S) \frac{d}{dz}(\mu_B - \mu_A) dz, \quad (9)$$

where δ is the interface thickness and the solid occupies the half-space $z < 0$. In the Hillert–Sundman model [11], $D(z)$ is assumed to vary exponentially across the interface, matching the solid and liquid values at the respective interface boundaries. Its prediction for the interfacial partitioning response function is obtained directly by evaluating the solution to the diffusion equation at $z = 0$ and $z = \delta$. Its prediction for the velocity-undercooling function is equivalent to that of equations (1) and (3), with ΔG_D given by equation (9) instead of (4). A similar analysis assuming a constant diffusivity (D_i) across the interface constitutes the two-level Baker model [12] as extended by us to predict both response functions.

1.2. Pulsed laser melting

Rapid solidification induced by pulsed-laser melting (PLM) is a well-controlled experimental technique for the study of interface response functions. A thin film geometry with samples with optically smooth surfaces and a spatially uniform laser readily effect plane-front solidification over the velocity regime of about 1–10 m/s.

The development of numerous time-resolved measurement techniques has permitted the quantitative analysis of the melting and solidification process [13–15]. The transient conductance measurement (TCM) technique uses nanosecond-resolved measurements of the transverse electrical resistance of a thin film on an insulating substrate. By exploiting the increase in electrical conductivity that accompanies Si melting, the crystal/melt interface velocity is measured during melting and subsequent solidification [13, 14]. A critical part of the work presented here is the development of a technique for time-resolved temperature measurements during rapid solidification induced by PLM. The technique [16–18] obtains temperatures by monitoring the time-dependence of the temperature-dependent resistance of a thin-film resistance temperature detector or “thermometer”, in close proximity to, but electrically insulated from, the alloy film. This allows for direct time-resolved measurements of the temperature at a fixed depth in the sample.

Using the TCM technique, the dilute alloy limit of

the CGM has been shown to describe the velocity dependence of the partition coefficient for several dopants in Si [6, 19–21], as well as for several alloying elements in Al [2, 22]. The objective of the current work is a complete test of models for both response functions of non-dilute alloys in a velocity regime chosen to distinguish between models with and without the solute drag effect.

1.3. The Si-As system

The Si-As system presents several advantages: interface velocity measurements are easy to perform in Si-based systems; the velocity-undercooling function for pure Si is well known [15, 23, 24]; virtually the entire range of k is readily accessible by PLM; and, because large As concentrations can be trapped in the Si lattice by PLM [25–27], the predicted effect of solute drag is substantial. As a first step [28], we studied the high-velocity limit in which $k \approx 1$ (partitionless solidification) and thereby determined Si-As alloy thermodynamic parameters required as input to kinetic models [8]. Earlier studies of Si-As resulted in significantly different values for the congruent melting temperature T_0 [27, 29, 30].

We will present measurements of the solute trapping and velocity-undercooling response functions for polycrystalline Si-4.5 at.% As and Si-9 at.% As alloys at velocities ranging from 0.25 to 2 m/s. These results provide a test of models for the velocity-undercooling function and for solute trapping beyond the dilute alloy limit. This complete experimental determination of both interface response functions for rapid alloy solidification allows us to address the controversy about solute drag effects in solidification. Preliminary results have been reported previously [31, 32]. We will show that the CGM without solute drag fits the velocity-undercooling and solute trapping measurements quite well, whereas the CGM with solute drag and all other solute drag models do not fit the data. The solute drag model of Hillert and Sundman (H–S) [7, 11] also predicts negligible solute drag in agreement with our measured undercoolings, but does not agree with the solute trapping data.

2. EXPERIMENTAL TECHNIQUES

2.1. Specimen preparation

A schematic drawing of the sample structure is shown in Fig. 1, while the sample layer structure and processing methods are shown in Table 1. A thin Pt layer placed between the Si-As alloy film and the Si substrate acts as a thermometer. The Pt film is electrically and thermally insulated from the Si substrate by an SiO_2 film and from the Si-As layer by a thin silicon nitride (SiN_x) film. The bare Pt films were annealed for 10 min at 800°C in flowing Ar. Due to the high temperatures achieved during laser irradiation, materials with high melting points (Si_3N_4 and Pt) were chosen for the layers that were not supposed to

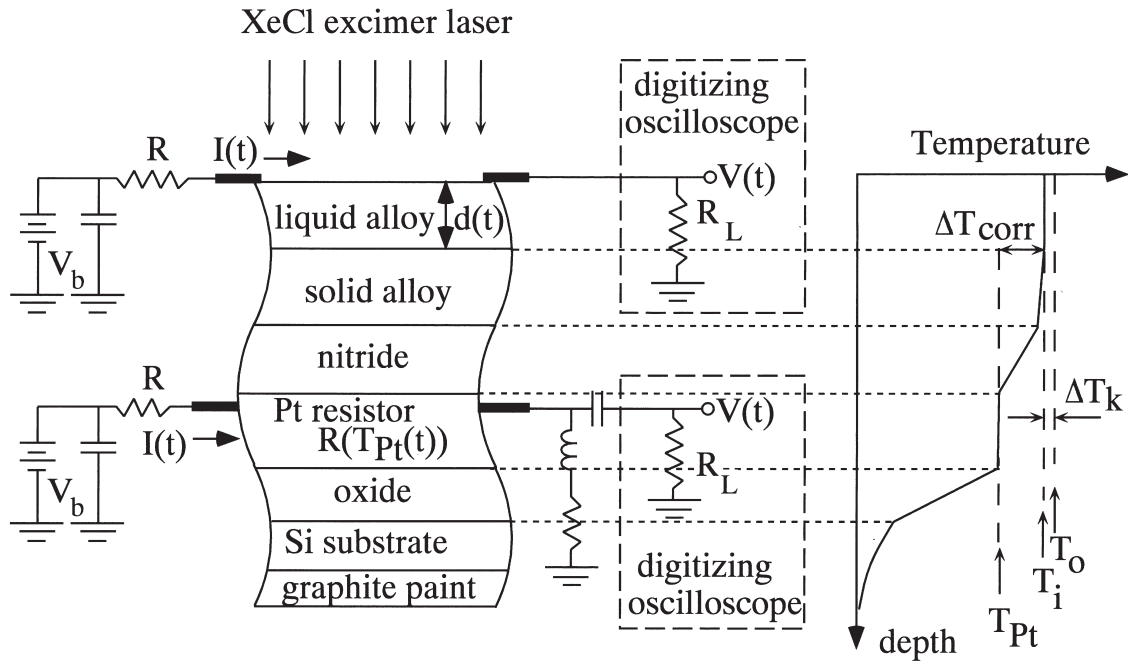


Fig. 1. Schematic cross section of sample structure. Transient lateral electrical conductance of alloy layer determines melt depth history $d(t)$ and solidification velocity $v(t)$; transient lateral electrical conductance of Pt layer, which never melts, determines time-resolved temperature $T_{Pt}(t)$ nearby. Temperature correction is performed to obtain temperature T_i of crystal/melt interface for quasistationary temperature-depth profile occurring during solidification, as shown schematically on the right. Layer thicknesses are reported in Table 1.

Table 1. Specimen structure

Layer	Processing method	Thickness (nm)
Si (001) wafer		$\sim 10^6$
SiO ₂	LPCVD ^a	110 or 1000
Pt	E-beam deposit	40
SiN _x	PECVD ^b	80
Si	E-beam deposit	250
Al contacts	Thermal deposit	400

^a Low pressure chemical vapor deposition.

^b Plasma-enhanced chemical vapor deposition.

melt. With these layers, the devices could be laser irradiated multiple times and yield reproducible measurements. The insulating layers act as the main thermal barriers controlling heat diffusion into the substrate, and thereby controlling the solidification velocity. The thicknesses of the insulating films were chosen to permit a range of v reaching high enough to ensure nearly partitionless solidification ($k \approx 1$), but not so high as to result in the growth of amorphous alloys at high As concentrations [33].

Photolithographic techniques were used to pattern resistors in the Si-As film for TCM and in the Pt film for temperature measurements. An optical micrograph of a device is shown in Fig. 2. The TCM resistors had a length to width (L/W) ratio of 32, and the Pt resistors had a L/W ratio of 20 and a room temperature resistance of $\sim 100 \Omega$.

Approximately flat As concentration-depth profiles in the top 150 nm of the Si films were obtained by

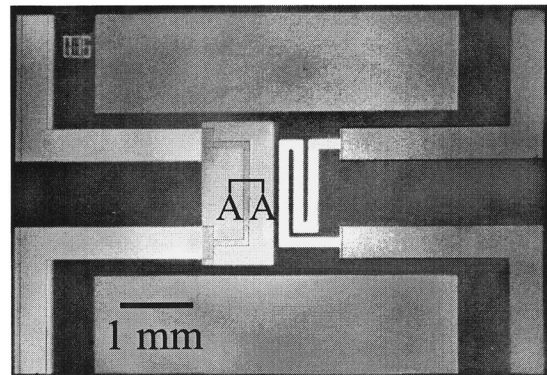


Fig. 2. Plan-view optical micrograph of device. Al contacts extend to the four corners. Pattern on right-hand side is alloy layer for measuring $d(t)$. Pattern on left-hand side is Pt layer under partially transparent alloy layer for measuring $T(t)$; Al contacts do not touch top alloy layer. Laser footprint is highly uniform over several mm in each direction. Cross section A-A is shown in Fig. 5.

implanting As⁺ at four different energies. Alloys with 4.5 at.% As in the top 150 nm were prepared with doses of $2.2 \times 10^{16}/\text{cm}^2$ at 200 keV, $9.2 \times 10^{15}/\text{cm}^2$ at 100 keV, $5.0 \times 10^{15}/\text{cm}^2$ at 50 keV and $3.0 \times 10^{15}/\text{cm}^2$ at 40 keV. Twice these doses were used for Si-9 at.% As alloys. Samples were annealed for 10 min at 700°C in flowing Ar to crystallize the Si-As layer.

2.2. Laser melting

Samples were irradiated (Fig. 3) using a 30 ns FWHM XeCl (308 nm) excimer pulse at energy densities ranging from 0.15 to 0.8 J/cm². The laser beam was spatially homogenized to within $\pm 5\%$ (homogenizer from XMR Inc.) to obtain uniform illumination of the samples. The samples were laser melted several (typically four) times to melt depths of ~ 150 nm in order to homogenize the As distribution by diffusion in the liquid state. For each device, homogenization was completed before data were collected for analysis. The peak melt depths were kept between 130 and 160 nm to ensure a uniform As concentration profile in the molten alloy and sufficient time for the interface to approach steady state conditions during solidification. To obtain a wider range of solidification velocities, some samples were preheated for a few seconds immediately before firing the excimer laser using an 80 watt, continuous-wave CO₂ laser (10.6 μ m). The back of the sample was coated with graphite paint to improve the coupling of the infrared radiation. With preheating to ~ 900 K the solidification velocities were reduced by a factor of ~ 3 to below 0.3 m/s.

Three different types of time-resolved measurements were performed during and following PLM: time-resolved reflectivity (TRR) measurements, TCM, and time-resolved temperature measurements. TRR measurements were made using a continuous-wave argon laser (488 nm) at grazing incidence with *p* polarization (Fig. 3). Large changes in the optical reflectivity of Si indicate melting or resolidification of the top ~ 4 nm. Melt durations from TRR were used to corroborate the melt profiles obtained from TCM.

The circuits used to measure the melt depth-dependent resistance of the Si-As resistor and the tempera-

ture-dependent resistance of the Pt thermometer are shown in Fig. 1. Suppression of signal reflections was accomplished with a traveling pulse configuration [17, 34] consisting of a pulse charge line impedance-matched with the power supply and a transmission line impedance-matched with the oscilloscope. The data were acquired with a high speed digitizing oscilloscope.

2.3. Characterization

Arsenic concentration profiles before and after PLM, as well as layer thicknesses, were determined by Rutherford backscattering spectrometry (RBS) using 2 MeV He⁺⁺ ions. A grazing exit angle geometry (75° from surface normal) was used to obtain a depth resolution of ~ 9 nm. The As profiles were approximately uniform in the top ~ 150 nm, with the As concentration decreasing with depth from there on. The As concentrations in the top 150 nm were measured to be 4.5 at.% and 9 at.% for the low and high dose implants respectively. The thicknesses reported in Table 1 were obtained from analysis of the RBS spectra.

Plan-view transmission electron microscopy (TEM) analysis was performed using a Philips 420 electron microscope at 120 keV. The samples were thinned by chemically etching the Si substrates in a solution of 20% HF in HNO₃, followed by ion milling with 3 keV Ar⁺ ions. X-ray diffraction studies were performed on the films in a θ - 2θ geometry with Cu K α radiation.

Cross-sectional TEM samples were prepared with a Hitachi FB-2000A focused ion beam (30 keV Ga⁺, 15 nA to 10 pA). First, a thick (150 nm) Au coating was deposited prior to the standard W coating to maintain the original surface for melt depth determination. Microscopy was performed on a Hitachi 8100 microscope operating at 200 keV.

3. DATA ANALYSIS

Both the partition coefficient and interface temperature versus interface velocity relations reported below are reported for an interface depth 30 nm from the surface, sufficiently far from the beginning of solidification for steady state to be established, but far enough away from the surface to prevent the proximity of the final transient from altering the steady state conditions. Results from numerical liquid diffusion and partitioning simulations for 9% As are in excellent agreement with the data, which indicate that the As concentration after solidification at 30 nm is ~ 9 at.% for most solidification velocities, but has slightly lower values ($\sim 8\%$) for the lowest solidification velocities. This slight velocity-dependence of X_S was taken into account in all model computations.

3.1. Partition coefficients

Partition coefficients during solidification were obtained by comparing concentration profiles after

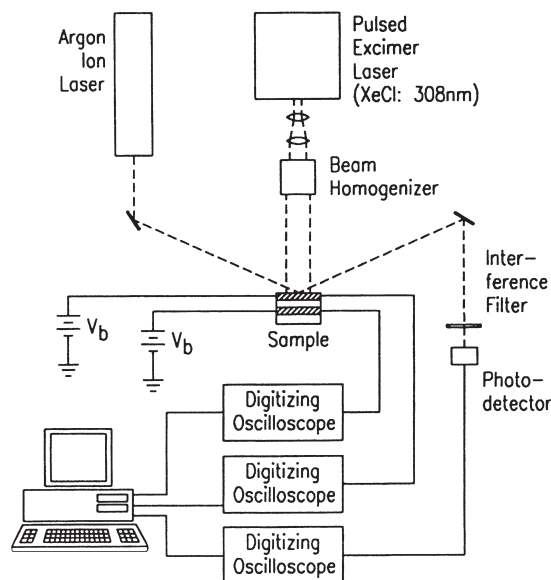


Fig. 3. Schematic of experimental setup showing optical and electrical signal propagation.

solidification with the results of numerical simulations of liquid diffusion and partitioning [19, 32]. Measured melt-depth history and initial concentration profiles were used as inputs. For each sample, there is a small range of solidification velocities relevant to the determination of k (v decreases slightly over the depth range of significance to the measurements). Simulating solidification over such a range of v requires an assumption about dk/dv . Although assuming $dk/dv = 0$ for any given sample results in a reasonable fit to the data, we used the slightly more accurate assumption that over the small velocity range sampled, k varies with v as predicted by the CGM (equation (7)): $dk/d \log v = (k - k_e)(1 - k)/(1 - k_e)$. This assumption about the local behavior of dk/dv does not result in any bias for the global $k(v)$ relation determined by fitting many samples covering a wide range of v .

3.2. Interface temperature

The Pt thermometer permitted us direct time-resolved measurements of the temperature in the solid near, but not at, the interface. These measurements were then used to determine the crystal/melt interface temperature during solidification [17]. In Fig. 1 we show a schematic plot of the temperature profile at a particular time during solidification, after the initial transient behavior setting up the interfacial undercooling has decayed away but before the start of the final transient behavior associated with the collision of the zone-refined solute boundary layer with the free surface. Because of its high thermal conductivity, the thin Pt film acts as a thermal short-circuit. Heat-flow simulations [28] show that the temperature profile during this stage of solidification is very uniform within the Pt film, with temperature differences of only a few degrees between the top and bottom interfaces. This permits a straightforward conversion from Pt resistance to Pt film temperature using the results of the calibrations described in this section.

During solidification, the interface temperature was determined from measured Pt resistor temperatures, T_{Pt} , using an approximate solution to the heat flow equation [17, 28, 31] in which

$$T_i = T_{Pt} + \Delta T_{\text{corr}}. \quad (10)$$

The sole heat source is the interface, moving at nearly constant velocity, and the only significant sink is the bulk of the solid. Hence the heat flux below the crystal/melt interface is nearly uniform with depth, temperature changes with time in the top layers are small during this part of the solidification stage, and

$$\Delta T_{\text{corr}} \cong v H_F \int \frac{-dz}{K(z)} \cong v H_F \left(\frac{d_{\text{insul}}}{K_{\text{insul}}} + \frac{d_{\text{alloy}}}{K_{\text{alloy}}} \right), \quad (11)$$

where the integration is performed from the top of

the Pt film to the crystal/melt interface, $K(z)$ is the position-dependent thermal conductivity, H_F is the enthalpy of fusion, K_{insul} and K_{alloy} are the thermal conductivities of SiN_x and the solid Si-As alloy, d_{insul} and d_{alloy} are the thicknesses of the SiN_x layer and the solid portion of the Si-As layer. No concentration dependence was found for H_F [28] and none is expected for the K at the high temperatures of interest here, so the pure Si values were used. Full numerical solutions of the time-dependent one dimensional heat equation [28] show that equation (11), which is the solution under steady-state conditions, is accurate to within ~ 10 K toward the end of solidification, and that the effect of the Pt layer on v is negligible.

The interface velocity for equation (11) is determined experimentally from the TCM data. To minimize ΔT_{corr} , the insulating SiN_x layer was kept as thin as possible while reliably isolating the Pt layer from the Si-As alloy electrically. K_{insul} was determined from measurements performed on pure Si combined with furnace calibrations as discussed below. The combination of TCM (to measure v) and thermometer measurements thus provide a determination of T_i during rapid solidification. Note that in this analysis no numerical heat-flow simulations are necessary to determine T_i , although they have been used to corroborate the approach taken here.

Time-resolved measurements on pure Si samples were used to determine K_{insul} . The interface temperature for Si is related to the melting temperature T_m by

$$T_m = T_i + \Delta T_k, \quad (12)$$

where ΔT_k is the kinetic interfacial undercooling. The velocity-undercooling relation is given by equation (1). For partitionless alloy solidification at small undercooling,

$$\Delta G_{\text{DF}} \cong -\frac{H_f \Delta T_k}{T_0}, \quad (13)$$

where T_0 is the congruent melting point, and in this case the kinetic undercooling is given by

$$\Delta T_k \cong \frac{RT_i T_0}{H_f} \frac{v}{v_0}. \quad (14)$$

For Si (001) near T_m , measured values of the “interface sluggishness”, $d\Delta T_k/dv$, range from 3 to 18 K s/m [15, 23, 24]. A value of 15 K s/m was used in the analysis. The quantity of primary interest for kinetic models is the *difference* between the interface temperature of the alloy and that of pure Si at the same v . The uncertainty in interface sluggishness has little effect on this quantity because any errors in interface sluggishness affect the velocity-undercooling func-

tions of the alloy and of pure Si in approximately the same way.

Because small variations in the room temperature resistance of the Pt thermometers were observed from device to device, furnace calibrations were performed on each device after laser irradiation and data collection. The thermometer resistance vs. temperature relation was measured in the range from room temperature to 450°C, over which the devices showed reproducible linear behavior. Higher temperature furnace treatments resulted in degradation as indicated by irreversible increases in resistance. Bare Pt films, however, showed linear reproducible behavior in furnace annealing up to 1000 K. A Pt temperature scale was first obtained using the results of furnace calibrations (linear fit and extrapolations). This was used to determine $K_{\text{insul}} = 0.017 \text{ Wcm}^{-1}\text{K}^{-1}$ from pure Si PLM data at high interface velocities (for which $T_{\text{Pt}} \sim 1050 \text{ K}$; see Fig. 4) using equation (11) and accounting for the known kinetic interfacial undercooling.

We require that as $v \rightarrow 0$, $\Delta T_{\text{corr}} \rightarrow 0$ and $\Delta T_{\text{k}} \rightarrow 0$ and therefore that $T_{\text{Pt}} \rightarrow T_{\text{m}}$ (equations (10), (11), (12), and (14)). However, for pure Si, the nominal $T_{\text{Pt}}(v)$ plot showed that the extrapolation of Pt temperature to $v=0$ undershot the melting point of Si by $\sim 10\%$. This was attributed to nonlinearities of Pt thin film resistance vs. temperature above 1100 K. A correction to the Pt temperature scale for temperatures above 1100 K was therefore determined using the Si data and assuming a linear relation between Pt temperature and interface velocity that extrapolated to the melting point of Si for $v = 0$. The same correction (determined from pure Si data only) was then applied to the Si-As alloy data. The effect of these calibration procedures was that the data from the pure Si samples served solely as a calibration of the temperature measurements for the alloys. The calibrated temperatures are shown in Fig. 4.

4. RESULTS

A cross-section of a laser melted Pt thermometer device (cross-section location indicated in Fig. 2) is

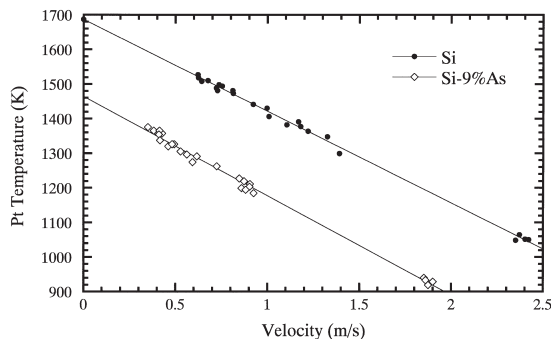


Fig. 4. Pt temperature vs. v . Data below 1100 K determined from furnace calibration and linear extrapolation. Data above 1100 K calibrated by requiring pure Si curve to pass through T_{m} at $v = 0$.

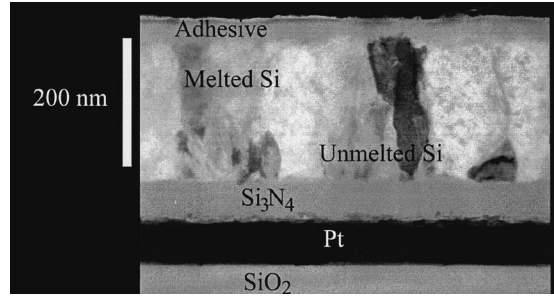


Fig. 5. Transmission electron micrograph of cross section A-A indicated in Fig. 2 of sample melted four times, showing maintenance of smooth interfaces and absence of degradation from melting and solidification.

shown in Fig. 5. The device was melted four times at a fluence and melt depth identical to those used in data collection. The polycrystalline Si-As layer is 210 nm thick. The deepest melt penetration is evident from the termination of some unmelted grains at a depth of $\sim 150 \text{ nm}$. Both the amorphous silicon nitride insulating layer and the Pt thermometer layers have relatively smooth interfaces and exhibit no damage from the laser melting process. Below the $1 \mu\text{m}$ thick SiO_2 layer, which extends beyond the bottom of the micrograph, is the Si substrate. This sample was produced in the same manner as those used in the data collection, although the batch from which the micrograph was prepared had slightly different layer thicknesses.

Plan-view TEM studies of samples solidified at 1.9 m/s showed that the resulting Si-As alloys were polycrystalline and homogeneous, with an average grain size of $\sim 300 \text{ nm}$ [35]. Diffraction rings indicated random orientations in the plane of the film, with no allowed orders of diffraction missing (indicating no strong texture in the direction normal to the substrate). X-ray studies showed good agreement between the relative intensities of the three most intense peaks and those expected for randomly oriented polycrystalline films [32].

Reflectivity vs. time traces in Fig. 6 show sharp transitions from the solid to the liquid reflectivity values upon surface melting, and slightly broader

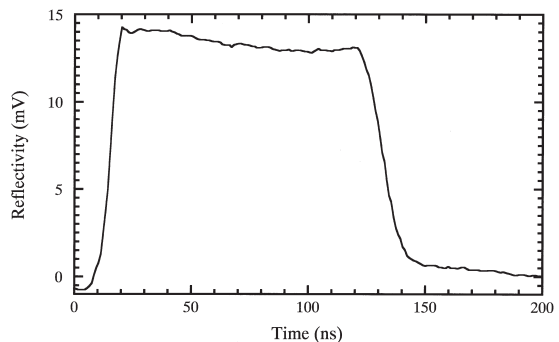


Fig. 6. Time-resolved reflectivity of Si-9 at.% As alloy showing sharp transitions when the surface melts and solidifies.

transitions at surface solidification. This suggests that the crystal/melt interfaces were approximately planar. The transitions at solidification, however, were broader than expected for perfectly planar interfaces. In the case of planar crystal/melt interface motion, the decay time τ_p for the reflectivity signal at solidification is approximately $(2\alpha v)^{-1}$ [36], where, in our case, α is the optical absorption coefficient of the Ar laser radiation divided by the cosine of the angular deviation of the refracted beam from normal. An estimate of the interface roughness σ is given by $2\sigma \approx v(\tau - \tau_p)$, where τ is the measured decay time of the reflectivity signal. We estimated $\sigma \sim 15$ nm. These small deviations from planar crystal/melt interface motion are most likely due to spatial inhomogeneities of the laser energy density or in the surface reflectivity due to the polycrystallinity, although differences in the melting and solidification velocities among grains with different orientation in the Si-As film may also be contributing factors.

Room temperature conductivities after PLM were independent of solidification velocity and indicated that As was quenched into electrically active sites. In addition, excellent matching was obtained between measured concentration profiles and results of solute liquid diffusion and partitioning simulations assuming planar interface motion. These observations, along with the TEM images, indicate that the interface was stable against morphological instabilities [37–40].

Diffusion coefficients (D_L) in the liquid Si-As alloys were determined by fitting simulated profiles for samples that underwent deep melts. For both 4.5 and 9 at.% As alloys, D_L was determined to be $(1.5 \pm 0.5) \times 10^{-4}$ cm²/s. In Fig. 7 we show concentration depth profiles before and after PLM for one sample and results of the corresponding liquid diffusion and partitioning simulation. The value of D_L is determined mainly by the amount of As penetrating to deeper depths during the melt period and is not very sensitive to the value of k in this regime; the value of k is determined mainly by the size of the

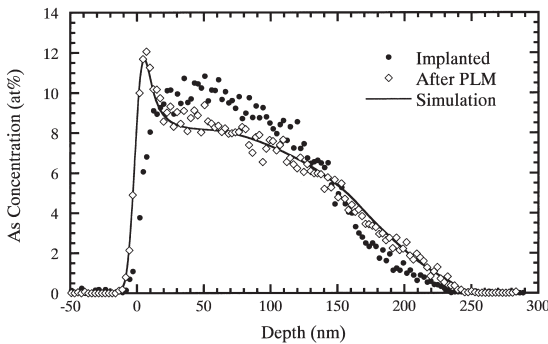


Fig. 7. Arsenic concentration-depth profiles for Si-9 at.% As sample before and after melting. Max. melt depth 240 nm; solidification velocity 0.62 m/s. Liquid diffusion and partitioning simulation using measured starting profile and measured interface position vs. time fits data well with $D_L = 1.5 \times 10^{-4}$ cm²/s and $k(0.62 \text{ m/s}) = 0.7$.

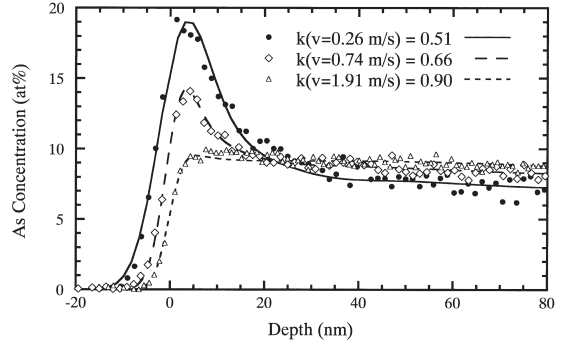


Fig. 8. Arsenic concentration-depth profiles focusing on surface peak of samples solidified with velocities of 0.26, 0.74, and 1.91 m/s. Points: experimental data; lines: simulation with $D_L = 1.5 \times 10^{-4}$ cm²/s and indicated values of partition coefficient.

“surface peak” which measures the amount of As swept back to the surface by the solidification front [6].

In Fig. 8 we show blow-ups of the surface peaks for three Si-9 at.% As samples spanning the range of measured solidification velocities used to extract the $k(v)$ relation. No evidence of a surface peak is observed for the sample solidified at the highest velocity. This resulted in a much larger uncertainty in k than for samples that exhibited a surface peak. In Fig. 9 we show the resulting experimental $k(v)$ response function for Si-4.5 and 9 at.% As.

In Fig. 10 we show the melt depth and Pt temperature traces measured simultaneously on Si-9 at.% As samples for three different v . The T_{Pt} scale was corrected above 1100 K as discussed above. The $T_{Pt}(v)$ results are shown in Fig. 4. The main feature observed when comparing the pure Si to the Si-9 at.% As data in Fig. 4 is a temperature shift with little or no change in slope. This observation alone will turn out to be sufficient to rule out most solute drag models. The resulting $T_i(v)$ response function is shown in Fig. 11.

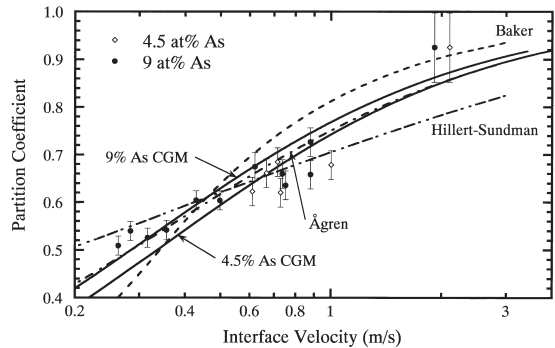


Fig. 9. Partition coefficient vs. interface velocity response function. Experimental data points for compositions indicated. Curves for various models. CGM: Continuous Growth Model, $v_D = 0.37$ m/s assumed composition-independent. Two-level Baker model: $v_D = 0.035$ m/s. Ågren model: $v_D = 0.065$ m/s. Hillert-Sundman model: interface thickness=73 nm.

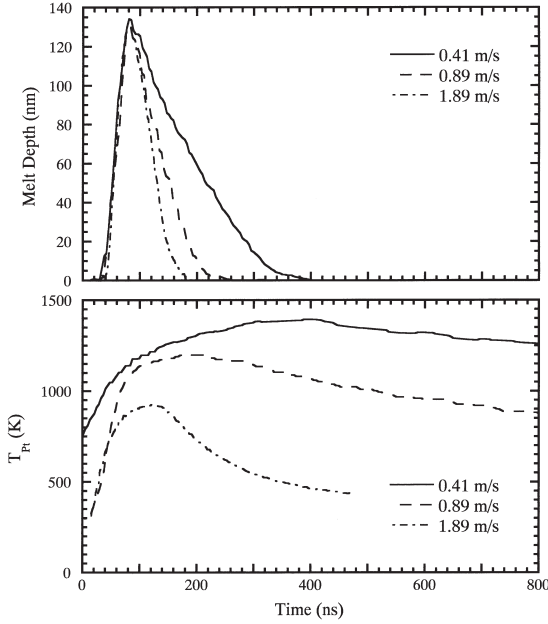


Fig. 10. Time-resolved melt depth and corresponding Pt temperature for Si-9 at.% As alloys. Velocity was varied by varying CO_2 preheat temperature and thickness of underlying oxide.

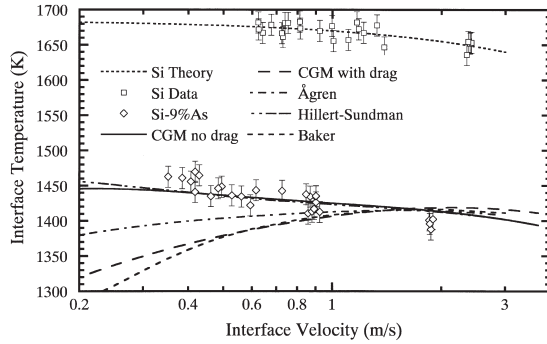


Fig. 11. Interface temperature vs. velocity response function. Theoretical pure Si curve taken from literature as discussed in text; calibration procedure forces pure Si data to fit curve. CGM without solute drag and Hillert-Sundman model fit alloy data; other models do not.

5. MODEL COMPUTATIONS

5.1. Thermodynamic parameters

We compared our results to the predictions of the CGM and Ågren sharp-interface models and the Baker and Hillert-Sundman diffuse-interface models. In all cases the free energy functions of liquid and supersaturated solid are required as input. A subregular solution model was used to compute the thermodynamic functions for the solid and liquid alloys, with the Gibbs free energy given by

$$G = XG_{\text{As}}^0 + (1-X)G_{\text{Si}}^0 + RT[(1-X)\ln(1-X) + X\ln X] + X(1-X)\Omega \quad (15)$$

where X is the mole fraction of As, Ω is an interaction parameter that was permitted to depend linearly on temperature, R is the gas constant, and G_{Si}^0 and G_{As}^0 are the Gibbs free energies for pure Si and pure As respectively (with diamond structure for the solid in both cases). It is not possible within the framework of the subregular solution model to fit all existing thermodynamic data for the Si-As system. For this reason, we chose a set of thermodynamic parameters (Table 2) that results in a good fit to the equilibrium liquidus [41], measured values of $H_{\text{F}}(X)$ [28], and measured congruent melting temperatures $T_0(X)$ [28]. This set of thermodynamic parameters does not result in a good fit to the assessed equilibrium solidus, but there are large discrepancies in reported solidus data [41]. This parameter set also gives an unlikely value, $k_{\text{e}} = 7 \times 10^{-4}$, of the dilute limit of the equilibrium partition coefficient. Although the commonly accepted value of $k_{\text{e}} = 0.3$ is based on scant experimental evidence,* it is unlikely to be off by orders of magnitude. An alternative set of thermodynamic parameters, which has been developed for dilute solutions [32], fits the assessed [41] equilibrium solidus data (which correspond in practice to the maximum reported equilibrium solubilities) and gives a dilute limit of the equilibrium partition coefficient of 0.3. However, it results in a substantial underestimate of the measured H_{F} and, most crucially, a substantial overestimate T_0 . It therefore cannot be used to predict accurate interface temperatures in the non-dilute alloys studied here.

The choice of G_{As}^0 is somewhat arbitrary. It was chosen to fall within a range of reasonable values [27]; our conclusions are insensitive to the value within this range. The temperature-dependence of the interaction parameter for the solid (B in Table 2) was $151 \text{ J mol}^{-1} \text{ K}^{-1}$ for the CGM and H-S models, $145 \text{ J mol}^{-1} \text{ K}^{-1}$ for the Baker model and $146 \text{ J mol}^{-1} \text{ K}^{-1}$ for the Ågren model, chosen in each case to optimize the fit of the kinetic model to the experimental data. For the continuum (H-S and Baker) models, the parameters Ω , and in equation (15), which go into the determination of the chemical potentials in equation (8), are assumed to vary linearly across the interface and match the corresponding solid and liquid values at the boundaries.

Table 2. Thermodynamic parameters for Si-As. T is the absolute temperature in Kelvin

	Solid (diamond cubic)	Liquid
G_{Si}^0 (J/mol)	0	$50626 - 30 T$
G_{As}^0 (J/mol)	0	$-30 T$
Ω (J/mol)	$-195500 + B T$	$-140000 + 87.5 T$

* Olesinski and Abbaschian [41] report that the dilute limit of k_{e} is quoted by Burton [42] as 0.3, citing Hall [43] and J. D. Struthers, but that Hall actually reported a k_{e} smaller by a factor of five.

The two kinetic parameters are v_C and v_D (v_D is given by D_i/δ in the Baker model), except in the H–S model where v_D is replaced by the interface thickness δ as a parameter. For all models, the parameter v_C has a negligible effect on the $k(v)$ relation and was taken from the interface sluggishness for pure Si ($d\Delta T_k/dv = 15$ K s/m) to be $v_C = 31$ m/s; our conclusions are not sensitive to the value of v_C within the range [24] of reported values. The remaining kinetic parameter was determined by fitting the $k(v)$ data. For the H–S model we used $D_S = 1 \times 10^{-13}$ cm²/s for the diffusivity in the solid alloy at the interface [44, p. 422], corresponding to measured T_i of ~ 1420 K, and $D_L = 1.5 \times 10^4$ cm²/s obtained experimentally from the present study.

5.2. Comparison with models

Our strategy for comparing the models to the data was to fit the measured $k(v)$ relations to the data to determine the free parameter v_D or δ , and then to use this best-fit parameter value in predicting interfacial undercoolings to compare with the $T_i(v)$ data. The best-fit $k(v)$ relations for Si-9 at.% As predicted by the models, as well as the CGM $k(v)$ relations for other compositions, are superposed on the data in Fig. 9. The CGM without solute drag, equations (1), (2), and (5), describes the data very well with $v_D = 0.37$ m/s, and also is consistent with the observed negligible concentration dependence of the $k(v)$ relation. In the computations, the same value of v_D was used for both As concentrations. It should be noted, however, that the diffusive speed is defined theoretically in terms of a thermally activated diffusive jump at the interface [8]. Because T_i for the Si-9%As alloys is ~ 100 K lower than for the Si-4.5 at.% alloys, a slightly smaller value of v_D might be expected for the more concentrated alloy. The predictions of the Ågren model for $k(v)$ are virtually indistinguishable from those of the CGM.

We also implemented the continuum (Hillert–Sundman and two-level Baker) models and computed their predictions. The only difference between these models in our implementation is the $D(z)$ profile, which is an exponential function connecting the bulk solid and liquid values in the H–S model and an adjustable constant D_i in the two-level Baker model (see Fig. 13(a)). The two-level Baker model predicts slightly too steep a rise in k with $\log v$ to fit the data. In the dilute limit, $k(v)$ in the CGM, Ågren, and two-level Baker models is a function solely of the dimensionless ratio v/v_D and therefore in a plot of k vs. $\log v$, such as Fig. 9, the only effect of varying v_D is a rigid horizontal shift of the curve with no change in slope. For alloys of up to 10 at.% this statement also remains true to a good degree of approximation. Hence the slopes $dk/d \log v$ in Fig. 9 are parameter-independent and the too-steep slope of the two-level Baker model appears to be a general property that has prevented it from fitting $k(v)$ data in other systems as well [19]. Although we did not implement it, the orig-

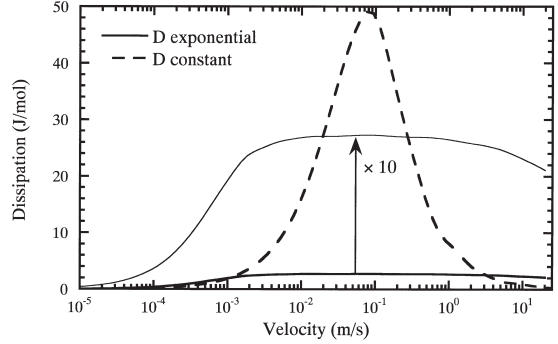


Fig. 12. Free energy dissipated per mole solidified for dilute solution ($X_S=0.01$) H–S model for assumed profiles of solute diffusivity and $\mu'_B - \mu'_A$ shown in Fig. 13(a). Case of “ D constant” is equivalent to two-level Baker model. Maximum dissipation for exponential diffusivity profile is only $\sim 5\%$ of that for constant-diffusivity profile.

inal Baker model [12] has a preferential solute adsorption site in the middle of the interface (a “third level”) and, with the associated pair of additional adjustable parameters, no doubt could fit the $k(v)$ data.

For the H–S model the best-fit value of the interface thickness was $\delta = 73$ nm. The calculated k vs. v curve perhaps rises slightly too slowly compared to the data, but the main drawback of the model is the unacceptably large value of δ required to fit the data. Furthermore, a reduction of δ by two orders of magnitude to a physically reasonable value produces a shift of the curve to the right by two orders of magnitude. Calculations with the H–S model and a dilute solution parameter set [32] (which cannot match the measured temperatures), result in similar predictions to those obtained for $k(v)$ with the parameter set used here except they result in a significantly smaller value of $dk/d \log v$ and a best-fit interface thickness of 6.2 nm — still an order of magnitude too large to be physically plausible. We have found no thermodynamic parameter set for which the H–S model with a physically plausible interface thickness fits the $k(v)$ data.

The results of the calculations of T_i are superposed on the data in Fig. 11. The H–S model and CGM without solute drag predict $T_i(v)$ relations in excellent agreement with the data. The Ågren, CGM with solute drag and two-level Baker models predict an increase in T_i with v over the range of v covered by the experiment, in conflict with the experimental results. Although we did not implement it, we expect that the original, three-level Baker model would fare no better than the two-level Baker model in this test. Because the free energy dissipated by solute-solvent redistribution is calculated and subtracted from the free energy driving interface motion before the interface velocity is determined, in principle the H–S and Baker models are solute drag models. However, the actual magnitude of the solute drag effect computed from the H–S model is negligible and that from the

Baker model substantial, for reasons to be discussed below.

Combining the $k(v)$ and $T_i(v)$ measurements results in a complete experimental determination of the interface response functions for rapid alloy solidification and allows us to critically test the models. The CGM without drag fits the data for both the $k(v)$ and $T_i(v)$ relations. None of the other models, all of which are solute drag models, fit both the $k(v)$ and $T_i(v)$ data.

6. DISCUSSION

6.1. Solute trapping models and parameters

The diffusive velocity determined from the CGM for the Si-As system was $v_D = 0.37$ m/s, which is nearly two orders of magnitude lower than that determined for the Si-Bi system ($v_D = 32$ m/s) [19]. Virtually indistinguishable predictions for $k(v)$ result from calculations using the CGM with $v_D = 0.46$ m/s and a different thermodynamic parameter set (Parameter Set 1 of [32], optimized for dilute solutions but inaccurate for concentrated solutions). Either value is consistent (although as an extreme) with a trend observed for several Si as well as Al alloys, for which an inverse correlation is found between v_D and k_c [3, 22]. It has been suggested that kinetic barriers for solute-solvent redistribution across the interface are smaller for systems with steep potential gradients and that the quantity $v_D \times k_c^{1/2}$ is approximately the same for different solutes in the same solvent [3, 22]. This relation is approximately followed in the existing data for (001) oriented Si alloys [3, 19, 21]. Although the predictions of the Ågren model for $k(v)$ are virtually indistinguishable from those of the CGM, the value of $v_D = 0.065$ m/s required to fit the data is quite different. Because the CGM and Ågren models for $k(v)$ are virtually identical except for a subtle difference in the flux-driving force relationship at large driving force, which is not directly measurable, this observation indicates a very sensitive model-dependence to the v_D values inferred from solute trapping measurements and should act as a warning against over-interpreting inferred v_D values.

The extension of the CGM to treat step-flow growth is called the Aperiodic Stepwise Growth Model (ASGM) [45]. The predictions of the ASGM and the CGM are virtually indistinguishable for both the $k(v)$ and the $T_i(v)$ behavior. The ASGM postulates that the kinetic processes described by the CGM occur at step edges during lateral step motion rather than at a rough interface, so if only a single orientation is under consideration then the same equations describe step motion in the ASGM and interface motion in the CGM and the main difference is the effective diffusive speed. Subsequent solute-solvent redistribution through the terrace is independent of the step motion in the ASGM and causes an insignificant change in driving free energy in the regime

covered by the experiment. Additionally, it has been shown [32] that for polycrystalline samples such as those used here, the orientationally-averaged ASGM and the CGM are virtually indistinguishable for $k(v)$. Hence if we are interested in only the velocity-dependence of k and T_i and not the orientation-dependence, the CGM and ASGM perform equally well. Measurements of the orientation-dependence of T_i must await the availability of single crystal thin films of variable orientation on insulator substrates. In light of the success of the ASGM in describing the orientation-dependence of partitioning in Si [3, 45], clearly the CGM gives only an approximate description in this system; yet the approximate description works remarkably well. The CGM adequately describes the $k(v)$ relation in all systems in which it has been tested: single crystal Si, polycrystalline Si, and (111)-textured polycrystalline Al. Its advantage over the ASGM is its simplicity — it has only one instead of two free parameters — and its applicability to a wide range of materials systems. Additionally, although correlations, discussed above, have now been identified that help in estimating the values of the fitting parameters of both models in the absence of a solute trapping measurement [2, 3], the correlation for the CGM has been established for a wider range of systems than those for the ASGM.

6.2. Absence of solute drag

The absence of solute drag in alloy solidification, or its negligible value, can be inferred from the experimental results in a quite direct way, eliminating the need to assume specific values for several thermodynamic parameters as was done in the sections above. The characteristic feature for models that include a large solute drag effect such as the CGM with solute drag, Baker, and Ågren models, is that they predict, for constant X_S and velocities in the vicinity of v_D , a more positive slope on the $T_i(v)$ relation for the alloy samples than for pure Si [5]. In particular, for the lower interface velocities measured in our experiment, a large positive slope of $T_i(v)$ is predicted (Fig. 11), in contrast to the negative slope for the pure Si case. In contrast, the CGM without solute drag and Hillert-Sundman model (with negligible solute drag) predict similar (and negative) $T_i(v)$ slopes for the alloy and pure Si samples, even at the lowest velocities measured. These observations are quite general, and qualitatively insensitive to the choice of values for G_{Si}^0 , G_{As}^0 , Ω and $v_C(T_i)$ (or interface sluggishness) within reasonable ranges. The raw data show a nearly identical (and even slightly more negative) slope of $T_p(v)$ for the alloy than the Si samples for all velocities measured (Fig. 4). In order to reach the conclusion that the solute drag effect is negligible or non-existent, it is necessary to assume only that the thermal conductivity in the integrand in equation (11) does not increase strongly with temperature. A sufficiently strong increase would invalidate the analysis of the alloy samples using the high-

temperature value of K_{insul} obtained from the analysis of the pure Si samples. The magnitude of the possible error arising from this effect was evaluated by performing heat-flow simulations [28] varying the T-derivative of K_{insul} . The results of these calculations, using a composition-independent H_F , indicate that for our conclusions to be unaffected it suffices to assume that K_{insul} increases by less than 60% over the range 1000–1600 K. This requirement can be relaxed if the heat of fusion for the alloy is less than that of pure Si; however, our measurements indicate identical heats of fusion [35]. Existing measurements of thermal conductivity for Si_3N_4 show no increase but, taking the extremes of the error bars, we can safely assume an increase of less than 42% over this temperature range [46]. It then follows, through equation (11) or through full numerical heat flow simulations, that the slope of T_i vs. v for alloy samples is similar to that of pure Si over the experimental range, directly ruling out the models with significant solute drag effects.

6.3. Origin of solute drag effect

We have been unable to make any solute drag model, for either a sharp or a diffuse interface, reproduce both the measured $k(v)$ and $T_i(v)$ interface response functions quantitatively. In contrast, solute drag models have been successful at describing the interface response in the migration of grain [47] and anti-phase [48] boundaries. Each of the models discussed in this paper is of broad potential applicability — the models have been applied to solidification, solid-state transformations [49], and grain boundary migration [11] — and no reason is obvious for success in describing one growth process and failure in another. One possible explanation is that the effective driving free energy that goes into equation (1) is given by equation (2) for solidification and equation (3) for the migration of grain and anti-phase boundaries, and different “universality classes” must be identified to determine which equation is to be used. Alternatively, equation (3) may always be valid but with ΔG_D merely negligible for solidification. A potential explanation consistent with the latter possibility may be found from a closer examination of the origin of free energy dissipation due to solute drag in the Hillert–Sundman model. In Figs 12 and 13 we compare calculations for the H–S model using two different diffusivity profiles across the interface, using the parameters reported in Table 3. The dashed curves labeled “ D constant” result from the assumption of a spatially-uniform $D(z)$ across the interface (equivalent to the two-level Baker model). The solid curves labeled “ D exponential” result from the assumption that $\log D(z)$ varies linearly across the interface and has vastly different values on the two sides of the interface. Both of these profiles are shown in Fig. 13(a). A dilute solution ($X_S = 0.01$) is used for simplicity. Both cases assume the same linear variation (Fig.

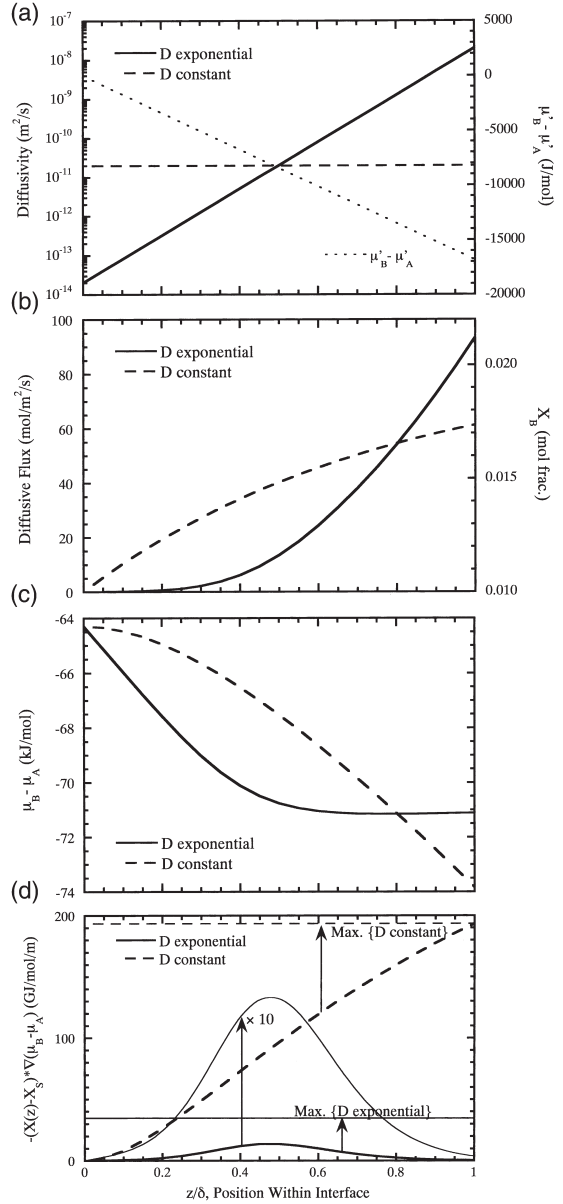


Fig. 13. Hillert–Sundman model, variation across interface of solute drag-related quantities at $v = 0.1$ m/s (peak dissipation in Fig. 12). (a) contrasting assumptions of $D(z)$ exponential and $D(z)$ constant, the latter being equivalent to the two-level Baker model. Both cases assume the same energetic bias for solute–solvent redistribution (dotted line). (b) Diffusive flux (left axis) and X_B (same curve measured along right axis; note scale starts at bulk solid composition), related by equation (16). Note flux kinetically frozen out near left-hand side for D exponential. (c) Chemical potential difference between B and A; note negligible gradient in right half for D exponential. (d) Integrand in equation (17), dissipation due to solute drag, obtained from curves in (b) and (c). Curve for D exponential is low on left due to (b) and high on right due to (c). Horizontal lines: values resulting from equation (17) by replacing position-dependent values in (b) and (c) with maximum value in the interface.

Table 3. Parameters used in calculations for Hillert–Sundman model ($\log D(z)$ varies linearly from $\log D_L$ to $\log D_S$) and 2-level Baker model ($D(z) = D_{\text{constant}}$) in this section

Parameter	Variable (units)	Value
Equilibrium partition coefficient	k_e	0.3
Solute concentration in solid at interface	X_s	0.01
Interface temperature	T_i (K)	1683
Atomic volume	Ω (m ³)	1.1×10^{-5}
Interface thickness	δ (m)	5×10^{-10}
Diffusivity for 2-level Baker model	D_{constant} (cm ² /s)	2×10^{-7}
Liquid diffusivity for H–S model	D_L (cm ² /s)	2×10^{-4}
Solid diffusivity for H–S model	D_S (cm ² /s)	2×10^{-10}

13(a)) of $\mu'_B - \mu'_A$ across the interface, where “A” is solvent, “B” is solute, and $\mu'_{A,B}(T) \equiv \mu_{A,B}(X_{A,B}, T) - RT \ln X_{A,B}$ is the redistribution potential representing energy plus local entropy but excluding the ideal entropy of mixing. The assumption of a linearly varying $\mu'_B - \mu'_A$ across the interface and that of linearly-varying Ω , G'_A and G'_B values (cf. Table 2) are equivalent for dilute solutions, but the former is simpler. The velocity-dependence of ΔG_D , the amount of free energy dissipated by solute–solvent redistribution within the interface, per mole of alloy solidified is shown in Fig. 12. Both models predict a peak at the same velocity, 10^{-1} m/s, because the diffusivity in the constant- D model has been chosen for convenience so that average value of $\log D$ is the same in both cases. (To apply the constant- D model to solid–solid transformations we might expect to use a lower value of $\log D$ resulting in a shift of the dashed curve in Fig. 12 to the left.) In Fig. 13(b–d) we consider the variation across the interface of relevant quantities, in each case for the velocity of maximum free energy dissipation, $v = 10^{-1}$ m/s (Fig. 12). The diffusive flux $j_d(z)$ and the mole fraction $X(z)$ of solute, both shown in Fig. 13(b), are related by [8]

$$j_d(z) = \frac{v}{V_m} [X(z) - X_s], \quad (16)$$

where V_m is the molar volume, and are found by solving equation (8) for $X(z)$. The resulting chemical potential difference between solute and solvent is shown in Fig. 13(c). The solute drag force on the interface, or the free energy dissipated by the interface, can be obtained by combining the quantities in Fig. 13(b) and (c). Aziz and Kaplan [8] showed that for diffuse interface models the total force P_{TOT} due to *both* solute and solvent species, per unit area of interface, is given by

$$P_{\text{TOT}} V_m = -(\Delta G_{\text{DF}}) + \int_0^\delta (X(z) - X_s) \frac{d(\mu_B - \mu_A)}{dz} dz \quad (17)$$

where $-\Delta G_{\text{DF}}$ (equation (2)) is positive for solidification and the integral, which is negative, is the product of the solute drag force/area and V_m . This integral is, within a minus sign, precisely the right-hand side of equation (9) for ΔG_D in a continuum model, i.e. the free energy dissipated by solute–solvent redistribution per mole of alloy solidified. The integrand, plotted in Fig. 13(d), is the product of factors determined in Fig. 13(b) and (c). Substituting ΔG_D for the integral, equation (17) should be compared with Equation (3) for sharp interfaces.

Now consider a position z_0 near the center of the interface in the profiles resulting from the model with a large diffusivity gradient, and contrast these profiles with those for uniform diffusivity. Slightly to the left of z_0 , D is so small that the diffusive flux is essentially shut off: $X(z) - X_s$ and $j_d(z)$ are essentially zero, as shown in Fig. 13(b). Slightly to the right of z_0 , D is so large that local equilibrium extends the rest of the way to the leading edge of the interface and the driving force for redistribution vanishes, i.e. $\mu_B - \mu_A$ must be flat as shown in Fig. 13(c). So z_0 marks the center of a narrow dissipative zone where the product of the diffusive flux and its conjugate driving force [8], $d/dz (\mu_B - \mu_A)$, is greatest (though still very small). Outside the dissipative zone, either the vanishing diffusive flux or the vanishing driving force ensures a negligible contribution to the integral in equation (17). Changing v shifts the center of the dissipative zone but does not significantly increase the width or the height of the curve in Fig. 13(d), resulting in a broad maximum in the solid curve in Fig. 12. Hence for sufficiently narrow dissipative zones, the total force on the interface due to both species in equation (17) is indistinguishable from $-\Delta G_{\text{DF}}$. This might be thought of as the diffuse-interface justification of equation (2), the no-solute-drag sharp-interface model that appears to accurately describe solidification. For grain boundaries and especially for anti-phase boundaries we expect a much less severe diffusivity gradient, resulting in a wider dissipative zone and hence the solute drag effect may be significant. In Fig. 13(d) the integrand in equation (17) is compared to the result, represented by the horizontal lines, that one would obtain from replacing each factor in the integrand with its maximum value in the interface. This operation represents, roughly speaking, what one does when replacing the diffuse interface model with the sharp-interface CGM with solute drag [8], as can be seen by comparing equations (4) and (9). It is seen that for the large diffusivity-gradient case, the resulting change is quite substantial. One can thereby

see why the CGM with solute drag predicts such a large solute drag effect compared to the Hillert–Sundman solute drag model. It is not fair, however, to characterize the CGM with solute drag as merely a less accurate approximation of the Hillert–Sundman model: in the case of a truly atomically sharp interface, one cannot define the variables in Fig. 13 other than at the endpoints, but the sharp-interface description inherent in the CGM still survives.

Apparently we can rationalize the negligible drag effect observed experimentally in two ways:

1. It is explained by a diffuse-interface picture with dissipation reducing v as envisaged by Hillert and Sundman but which, for a very large diffusivity gradient, naturally results in a negligible drag effect.
2. It is explained by a sharp interface picture such as the CGM without drag, in which the velocity of interface motion is not dependent on the free energy dissipation due to solute-solvent redistribution. That is, equations (1) and (2) result in $v \propto \Delta G_{DF}$ rather than $v \propto P_{TOT} V_m$, the entire r.h.s. of equation (17) [8].

On the one hand, no model based on the diffuse-interface concepts in (1) has yet been shown to agree quantitatively with both measured interface response functions for alloy solidification; however, this goal may yet be attainable. On the other hand, although the CGM without drag gives a quantitative fit to the data, it cannot explain the behavior of other apparently sharp interfaces, such as grain boundaries, in which the solute drag effect appears to be present. In this case we are left with a troubling arbitrariness of whether or not the solute drag effect “exists” as we consider a wider variety of boundary-motion problems.

We note that the CGM both with and without solute drag, as well as the other models discussed here, satisfy the requirements of the thermodynamics of irreversible processes for small, coupled driving forces. The free energy dissipation rate can be shown to be the sum of the products of the atomic fluxes J_i and their conjugate driving forces $\Delta\mu_i$ [8]: $dG/dt = J_A \Delta\mu_A + J_B \Delta\mu_B$. The key difference among models is in the postulated relationship between interface velocity and the various forces and dissipation terms [8]. Hillert takes issue with the resulting asymmetric cross terms in the coupling of fluxes to driving forces in the CGM without drag and therefore characterizes the model as being “of doubtful value” [49]. Although such asymmetric couplings are admittedly curious, they are permissible for models such as this one, to which Onsager’s reciprocity relations are inapplicable [50]. Finally, it should be noted that the CGM without drag assumes zero diffusion in the growing phase, that no model permitting diffusion in the growing phase has been developed to the point where it can be compared with experiment, and that Onsager’s

reciprocity relations put requirements on the response functions predicted by such models even when no such requirements exist on corresponding models without diffusion in the growing phase [50].

7. SUMMARY

The $k(v)$ and $T_i(v)$ interface response functions have been measured for non-dilute Si-As alloys using the behavior of pure Si as a calibration.

The CGM without solute drag, equations (1), (2), and (5), fits the data for both response functions. The kinetic parameters for this model are $v_D = 0.37$ m/s, obtained by fitting the $k(v)$ data, and $v_C = 31$ m/s, obtained from the literature for pure Si.

The Hillert–Sundman model fits the $T_i(v)$ data and, approximately, the $k(v)$ data, but in the latter case requires an interface thickness that is two orders of magnitude too high to be physically plausible.

We have been unable to make any solute drag model, for either a sharp or a diffuse interface, reproduce both the measured $k(v)$ and $T_i(v)$ interface response functions quantitatively.

The Hillert–Sundman model predicts a negligible solute drag effect for solidification. The steep rise in diffusivity results, for the partial solute trapping regime, in a region of the interface (close to the solid) where solute-solvent redistribution is kinetically frozen and a region (close to the liquid) that is in local equilibrium with the liquid. This leaves only a narrow zone within the interface where free energy is dissipated by the solute-solvent redistribution, resulting in a negligible total dissipation.

Qualitatively, one can rationalize the negligible drag effect observed experimentally in one of two ways: (i) It is explained by a diffuse-interface picture with dissipation reducing v as envisaged by Hillert and Sundman but which, for a very large diffusivity gradient, naturally results in a negligible drag effect; (ii) it is explained by a sharp interface picture such as the CGM without drag, in which the velocity of interface motion is not dependent on the free energy dissipation due to solute-solvent redistribution. Quantitative agreement based on (i) is still lacking. While (ii) is supported by the data in this study and is consistent with all solidification studies of which we are aware, it cannot explain the behavior of other apparently sharp interfaces such as grain boundaries.

Acknowledgements—This research was supported initially by NSF-DMR-92-08931 and subsequently by NSF-DMR-97-27369. We thank Yucong Huang for performing some of the heat-flow simulations used to corroborate our interpretation of the data.

REFERENCES

1. Baker, J. C. and Cahn, J. W. *Acta Metall.*, 1969, **17**, 575.
2. Smith, P. M. and Aziz, M. J. *Acta Metall. Mater.*, 1994, **42**, 3515.

3. Reitano, R., Smith, P. M. and Aziz, M. J. *J. Appl. Phys.*, 1994, **76**, 1518.
4. Baker, J. C. and Cahn, J. W. *Solidification*. Am. Soc. Metals, Metals Park, Ohio, 1970 p. 23.
5. Aziz, M. J. and Boettinger, W. J. *Acta Metall. Mater.*, 1994, **42**, 527.
6. Aziz, M. J. *Metall. Mater. Trans. A*, 1996, **27**, 671.
7. Hillert, M. and Sundman, B. *Acta Metall.*, 1977, **25**, 11.
8. Aziz, M. J. and Kaplan, T. *Acta Metall.*, 1988, **36**, 2335.
9. Agren, J. *Acta Metall.*, 1989, **37**, 181.
10. Turnbull, D. *J. Phys. Chem.*, 1962, **66**, 609.
11. Hillert, M. and Sundman, B. *Acta Metall.*, 1976, **24**, 731.
12. Cahn, J. W., Coriell, S. R. and Boettinger, W. J. in *Laser and Electron Beam Processing of Materials*, ed. C. W. White and P. S. Peercy, Academic Press, New York, 1980, p. 89.
13. Galvin, G. J., Thompson, M. O., Mayer, J. W., Hammond, R. B., Pautler, N. and Peercy, P. S. *Phys. Rev. Lett.*, 1982, **48**, 33.
14. Thompson, M. O., Galvin, G. J., Mayer, J. W., Peercy, P. S. and Hammond, R. B. *Appl. Phys. Lett.*, 1983, **42**, 445.
15. Larson, B. C., Tischler, J. Z. and Mills, D. M. *J. Mater. Res.*, 1986, **1**, 144.
16. Thompson, M. O. *Mater. Res. Soc. Symp. Proc.*, 1988, **100**, 525.
17. Brunco, D. P., Kittl, J. A., Otis, C. E., Goodwin, P. M., Thompson, M. O. and Aziz, M. J. *Rev. Sci. Instrum.*, 1993, **64**, 2615.
18. Sameshima, T., Hara, M. and Usui, S. *Jpn. J. Appl. Phys.*, 1989, **28**, L2131.
19. Aziz, M. J., Tsao, J. Y., Thompson, M. O., Peercy, P. S. and White, C. W. *Phys. Rev. Lett.*, 1986, **56**, 2489.
20. Aziz, M. J., Tsao, J. Y., Thompson, M. O., Peercy, P. S., White, C. W. and Christie, W. H. *Mater. Res. Soc. Symp. Proc.*, 1985, **35**, 153.
21. Hoglund, D. E., Aziz, M. J., Stiffler, S. R., Thompson, M. O., Tsao, J. Y. and Peercy, P. S. *J. Crystal Growth*, 1991, **109**, 107.
22. Smith, P. M., Reitano, R. and Aziz, M. J. *Mater. Res. Soc. Symp. Proc.*, 1993, **279**, 749.
23. Thompson, M. O., Bucksbaum, P. H. and Bokor, J. *Mater. Res. Soc. Symp. Proc.*, 1985, **35**, 181.
24. Aziz, M. J. *Mat. Sci. Eng. A*, 1997, **226/228**, 255.
25. White, C. W., Wilson, S. R., Appleton, B. R. and Young, F. W. *J. Appl. Phys.*, 1980, **51**, 738.
26. Natsuaki, N., Tamura, M. and Tokuyama, T. *J. Appl. Phys.*, 1980, **51**, 3373.
27. Lee, K. R., West, J. A., Smith, P. M., Aziz, M. J. and Knapp, J. A. *Mater. Res. Soc. Symp. Proc.*, 1992, **205**, 301.
28. Kittl, J. A., Reitano, R., Aziz, M. J., Brunco, D. P. and Thompson, M. O. *J. Appl. Phys.*, 1993, **73**, 3725.
29. Peercy, P. S., Thompson, M. O. and Tsao, J. Y. *Appl. Phys. Lett.*, 1985, **47**, 244.
30. Baeri, P., Reitano, R., Malvezzi, A. M. and Borghesi, A. *J. Appl. Phys.*, 1990, **67**, 1801.
31. Kittl, J. A., Aziz, M. J., Brunco, D. P. and Thompson, M. O. *Appl. Phys. Lett.*, 1994, **64**, 2359.
32. Kittl, J. A., Aziz, M. J., Brunco, D. P. and Thompson, M. O. *J. Cryst. Growth*, 1995, **148**, 172.
33. Baeri, P. and Reitano, R. *Phys. Rev. B*, 1989, **39**, 13231.
34. M.O. Thompson, Ph.D. Thesis, Section 2.6, Cornell University, 1984.
35. Kittl, J. A., Reitano, R., Aziz, M. J., Brunco, D. P. and Thompson, M. O. *Mater. Res. Soc. Symp. Proc.*, 1993, **279**, 691.
36. MacDonald, C. A., Malvezzi, A. M. and Spaepen, F. J. *Appl. Phys.*, 1989, **65**, 129.
37. Mullins, W. W. and Sekerka, R. F. *J. Appl. Phys.*, 1964, **35**, 444.
38. Hoglund, D. E., Thompson, M. O. and Aziz, M. J. *Phys. Rev. B*, 1998, **58**, 189.
39. Greven, K., Ludwig, A. and Sahn, P. H. *J. Appl. Phys.*, 1999, **86**, 3682.
40. Warren, J. A. and Langer, J. S. *Phys. Rev. E*, 1993, **47**, 2702.
41. Olesinski, R. W. and Abbaschian, G. J. *Bull. Alloy Phase Diagrams*, 1985, **8**, 254.
42. Burton, J. A. *Physica*, 1954, **20**, 845.
43. Hall, R. N. *J. Chem. Phys.*, 1953, **57**, 836.
44. Shackelford, J. F. and Alexander, W. ed. *The CRC Materials Science and Engineering Handbook*. CRC Press, Boca Raton, Fla, 1992, p. 422.
45. Goldman, L. M. and Aziz, M. J. *J. Mater. Res.*, 1987, **2**, 524.
46. Touloukian, Y. S., Powell, R. W., Ho, C. Y. and Klemens, P. G. *Thermal Conductivity: Nonmetallic Solids, vol. 2*, IFI/Plenum, New York, 1970.
47. Drolet, J. P. and Galibois, A. *Acta Metall.*, 1968, **16**, 1387.
48. Krzanowski, J. E. and Allen, S. M. *Acta Metall.*, 1983, **31**, 213.
49. Hillert, M. *Acta Materialia*, 1999, **47**, 4481.
50. Kaplan, T., Aziz, M. J. and Gray, L. J. *J. Chem. Phys.*, 1993, **99**, 8031.